



OPEN ACCESS

EDITED BY

Yuyao Zhang,
ShanghaiTech University, China

REVIEWED BY

Johannes Lindemeyer,
University Hospital of Cologne, Germany
Jun Li,
ShanghaiTech University, China

*CORRESPONDENCE

Patrick Fuchs
✉ p.fuchs@ucl.ac.uk

SPECIALTY SECTION

This article was submitted to
Brain Imaging Methods,
a section of the journal
Frontiers in Neuroscience

RECEIVED 23 December 2022

ACCEPTED 28 March 2023

PUBLISHED 17 April 2023

CITATION

Fuchs P and Shmueli K (2023) Incomplete
spectrum QSM using support information.
Front. Neurosci. 17:1130524.
doi: 10.3389/fnins.2023.1130524

COPYRIGHT

© 2023 Fuchs and Shmueli. This is an
open-access article distributed under the terms
of the [Creative Commons Attribution License
\(CC BY\)](https://creativecommons.org/licenses/by/4.0/). The use, distribution or reproduction
in other forums is permitted, provided the
original author(s) and the copyright owner(s)
are credited and that the original publication in
this journal is cited, in accordance with
accepted academic practice. No use,
distribution or reproduction is permitted which
does not comply with these terms.

Incomplete spectrum QSM using support information

Patrick Fuchs* and Karin Shmueli

Department of Medical Physics and Biomedical Engineering, University College London, London, United Kingdom

Introduction: Reconstructing a bounded object from incomplete k-space data is a well posed problem, and it was recently shown that this incomplete spectrum approach can be used to reconstruct undersampled MRI images with similar quality to compressed sensing approaches. Here, we apply this incomplete spectrum approach to the field-to-source inverse problem encountered in quantitative magnetic susceptibility mapping (QSM). The field-to-source problem is an ill-posed problem because of conical regions in frequency space where the dipole kernel is zero or very small, which leads to the kernel's inverse being ill-defined. These "ill-posed" regions typically lead to streaking artifacts in QSM reconstructions. In contrast to compressed sensing, our approach relies on knowledge of the image-space support, more commonly referred to as the mask, of our object as well as the region in k-space with ill-defined values. In the QSM case, this mask is usually available, as it is required for most QSM background field removal and reconstruction methods.

Methods: We tuned the incomplete spectrum method (mask and band-limit) for QSM on a simulated dataset from the most recent QSM challenge and validated the QSM reconstruction results on brain images acquired in five healthy volunteers, comparing incomplete spectrum QSM to current state-of-the-art methods: FANSI, nonlinear dipole inversion, and conventional thresholded k-space division.

Results: Without additional regularization, incomplete spectrum QSM performs slightly better than direct QSM reconstruction methods such as thresholded k-space division (PSNR of 39.9 vs. 39.4 of TKD on a simulated dataset) and provides susceptibility values in key iron-rich regions similar or slightly lower than state-of-the-art algorithms, but did not improve the PSNR in comparison to FANSI or nonlinear dipole inversion. With added (ℓ_1 -wavelet based) regularization the new approach produces results similar to compressed sensing based reconstructions (at sufficiently high levels of regularization).

Discussion: Incomplete spectrum QSM provides a new approach to handle the "ill-posed" regions in the frequency-space data input to QSM.

KEYWORDS

QSM, compressed sensing, incomplete spectrum, dipole inversion, Fourier transform, regularization, magnetic susceptibility

1. Introduction

The magnetic susceptibility of tissue χ_m is related to perturbations in the magnetic field ΔB_0 through convolution with the unit dipole field. These local field perturbations can be calculated from the phase variations measured in gradient-echo magnetic resonance imaging (MRI). In theory, reconstructing the underlying magnetic susceptibility from the local field perturbations requires deconvolution with the unit dipole field or dipole kernel. This is an ill-posed inverse problem because the dipole kernel contains zeroes on a conical surface in the frequency domain which lead to streaking artifacts in quantitative susceptibility mapping (QSM).

Over the years many different approaches to regularize this ill-posed problem have been proposed (Wang and Liu, 2015; Deistung et al., 2017; Shmueli, 2020): from direct approaches such as thresholding the dipole kernel (Shmueli et al., 2009; Schweser et al., 2013), to using iterative reconstruction methods (Wu et al., 2012; Kee et al., 2017; Milovic et al., 2018; Polak et al., 2020), and, most recently, deep-learning-based approaches (Bollmann et al., 2019; Jung et al., 2020, 2022).

Our approach to deal with this ill-posed region in frequency domain is to remove the affected data from the reconstruction. The QSM field-to-source inversion algorithm then needs to handle reconstructing the susceptibility from data that are incomplete in frequency domain (k-space: the MRI frequency domain). Reconstructing images from incomplete k-space data is often performed using compressed sensing (CS), where prior information on the sparsity of the image, in a (wavelet) transform domain, is used to aid reconstruction.

In contrast to CS, our approach does not rely on the incoherence of aliasing artifacts, but, rather, on a priori knowledge of the image-space support (more commonly referred to as the mask) of our object. Reconstructing a bounded object from incomplete k-space data is a well posed problem (Fuks, 1963; Papoulis, 1975), and it was recently shown that this incomplete spectrum (IS) approach can be used to reconstruct undersampled MRI images with similar quality to compressed sensing approaches, as shown by Rhebergen et al. (1997) and den Bouter et al. (2021).

In the case of QSM, the support information required for this incomplete spectrum approach is readily available as a binary mask as it is almost always used to remove background field contributions, and can generally be calculated from the magnitude images, see, for example, Smith (2002), Schweser et al. (2017), and Kiersnowski et al. (2022). No additional assumptions or priors are needed for the proposed approach. Our objective is to reconstruct a full magnetic susceptibility distribution (with a known mask) from incomplete k-space data. Here, we aimed to test this approach in QSM using both a numerical phantom and data acquired in five healthy volunteers. We investigated the effect of using different masks and band-limits (defining the incomplete region in k-space) on the reconstructed susceptibility maps using a numerical phantom. Using the volunteer data we compared our approach to conventional QSM reconstruction algorithms.

2. Theory: incomplete spectrum QSM reconstruction

We use the method first proposed in den Bouter et al. (2021) for MRI image reconstruction, which is a conjugate-gradient-least-squares (CGLS) algorithm applied to solve the normal equation of a space-limited and frequency-restricted Fourier transformation. In other words, instead of using the inverse fast Fourier transformation (FFT) to invert the Fourier transform equation

$$k = Fx, \quad (1)$$

where k are the data in frequency domain, x are the data in image space and F is the (forward) Fourier transform, we limit the extent

of x (through a mask, or support matrix S_x in image space) and restrict the frequency components of k (through a band limit or support matrix S_k in frequency domain). Then our space-limited and band-limited Fourier transform equation is

$$S_k k = S_k F S_x x. \quad (2)$$

It is important to note that we choose the mask S_x such that $S_x x = x$, or, in other words, so that the mask contains the support of the data *whose frequency domain we are attempting to reconstruct*. The normal equation of this model can then be solved for x using CGLS, as described in den Bouter et al. (2021).

In QSM, the local field perturbations, Δb_0 are related to the underlying magnetic susceptibility distribution χ_m through convolution with a dipole kernel d , first shown by Salomir et al. (2003) and Marques and Bowtell (2005)

$$\Delta b_0 = d * \chi_m. \quad (3)$$

When transformed into frequency domain, this becomes an elementwise product according to the convolution theorem. This can be written as a matrix multiplication

$$b = F^H D F \chi, \quad (4)$$

where F is the forward Fourier transform matrix and $F^H (= F^{-1})$ is the inverse Fourier transform matrix, D is a diagonal matrix containing the Fourier transformed dipole kernel coefficients and b and χ are column vectors with the local field and magnetic susceptibility values, respectively.

One might think that it would be straightforward to compute the magnetic susceptibility by a simple deconvolution approach. However, this is, unfortunately, not possible as this inverse problem is not well posed because the dipole kernel D contains zeros on a conical surface in frequency domain. A simple approach to regularizing this problem is, for example, thresholding the kernel, i.e., replacing values in D that are too small with the signed threshold value, see Shmueli et al. (2009). Here, we use band limiting in the frequency domain to limit the frequency samples to include only the regions where the dipole kernel D has sufficiently large values, and the inverse is well-defined. Our initial equation for the susceptibility is

$$F \chi = D^{-1} F b, \quad (5)$$

where the susceptibility distribution χ is the source of the local magnetic field perturbations b . These are usually derived from the measured phase through multi-echo phase combination, phase unwrapping and background field removal, as described in Shmueli (2020), and as will be specified in the Section 3. Here, we space-limit (S_χ) and band-limit (S_k) Equation 5 as

$$S_k F S_\chi \chi = S_k v, \quad (6)$$

where $v = D^{-1} F b$ are our “input data” in the frequency domain. It is worth noting that the mask is strictly binary and a diagonal matrix in this formulation, which means $S_\chi S_\chi = S_\chi$. In QSM this requirement is achieved through the background field removal step, where all field contributions from susceptibility sources outside

of a pre-defined mask are removed from the (total) measured field perturbations (inside the mask). On the right-hand side of Equation 6 S_k excludes the ill-posed regions close to the cone at the magic angle. Therefore, we can relate our full discrete Fourier transform to the limited transform using

$$F\chi = FS_\chi\chi = S_kFS_\chi\chi + (I - S_k)FS_\chi\chi, \quad (7)$$

where I is the identity matrix, which leads to

$$F\chi = S_kv + (I - S_k)FS_\chi\chi. \quad (8)$$

Taking the inverse Fourier transform F^H of both sides gives

$$\chi = F^HS_kv + F^H[(I - S_k)FS_\chi\chi]. \quad (9)$$

Left multiplying Equation 9 with the mask S_χ , and transferring the second term to the left hand side gives

$$(I - S_\chi F^H[(I - S_k)FS_\chi])S_\chi\chi = S_\chi F^HS_kv. \quad (10)$$

It can be easily verified, as in [den Bouter et al. \(2021\)](#), that by defining the space-limited and band-limited discrete Fourier transform matrix $A = S_kFS_\chi$, the above equation simplifies to the normal equation

$$A^HA\chi = A^Hv. \quad (11)$$

Which can then be solved in a least squares fashion, see, for example, [Strang \(2019\)](#), so using, for example, a CGLS algorithm.

2.1. Comparison to compressed sensing QSM reconstruction

In compressed sensing the optimization problem typically has a cost function of the form

$$F_{CS}(\chi) = \|S_kv - S_kF\chi\|_2 + \lambda \|\Psi\chi\|_1, \quad (12)$$

where Ψ is an appropriate sparsifying (often wavelet) transform, first described for MRI by [Lustig et al. \(2007\)](#).

As is well known, any solution that minimizes the least squares function

$$F_{IS}(\chi) = \|S_kv - S_kFS_\chi\chi\|_2 \quad (13)$$

satisfies the normal Equation 11 as well. We can therefore use this form to compare the approaches. Here, we include the full expression for the space-limited and band-limited discrete Fourier transform matrix $A (= S_kFS_\chi)$ to illustrate its similarity with the compressed sensing framework. It should be noted that, though masking is often applied in iterative QSM reconstructions, this is the first time that the mask-based background field removal unique to QSM is leveraged to generate conditions through which the masking turns the problem into a well-posed integral equation.

To compare QSM reconstruction performance between the compressed sensing and incomplete spectrum approaches, we added the additional sparsity-promoting regularization term

$\lambda\|\Psi\chi\|_1$ to our incomplete spectrum optimization procedure (see Equation 12) in a “regularized incomplete spectrum” reconstruction. This was implemented in the Julia programming language using the “RegularizedLeastSquares” package, which is closely related to the MRI-specific work by [Knopp and Grosser \(2021\)](#). The sparsifying transform used in the “regularized incomplete spectrum approach” was a Daubechies wavelet with 2 vanishing moments (db2) ([Vonesch et al., 2007](#)), which is commonly used for this purpose ([Majumdar and Ward, 2012](#)).

3. Methods

3.1. Numerical phantom

To validate the incomplete spectrum QSM reconstruction method, we used a numerical phantom. This means that there was a known ground-truth susceptibility distribution so the QSM reconstruction error could be computed. Rather than using a reconstructed susceptibility map as a ground truth (which could lead to an “inverse crime” ([Marques et al., 2021](#)), we used the QSM reconstruction challenge 2.0 dataset from the [QSM Challenge 2.0 Organization Committee et al. \(2021\)](#) (see [Figure 2](#)), simulated using a comprehensive model.

The input to this method was the Sim2 dataset’s local field map with signal to noise ratio SNR1. As the unwrapped, local field map was available, no additional pre-processing (i.e., background field removal) was necessary for susceptibility calculation. The brain mask used was the ground-truth mask provided with the dataset.

3.2. In vivo MRI acquisition

Since the simulated phantom is a high-resolution, high SNR data set, we also tested the performance of the incomplete spectrum method using brain images acquired *in vivo*. The *in vivo* dataset used is from [Karsa et al. \(2019\)](#), a gradient recalled echo acquisition at 3 Tesla with 1 mm isotropic resolution in five healthy volunteers. This was a 5 echo acquisition with echo times $TE_1 = 3\text{ms}$, 5.4 ms echo spacing, 20° flip angle, $TR = 29\text{ms}$, and pixel bandwidth = 270 Hz. Before susceptibility calculation, these data were processed according to the pipeline described in [Karsa et al. \(2019\)](#), described briefly here: the total field map was calculated from the multi-echo data using non-linear complex fitting ([Liu et al., 2013](#)). The total field map was then unwrapped using Laplacian unwrapping ([Schweser et al., 2013](#)), followed by background field removal with projection onto dipole fields (PDF) ([Liu et al., 2011](#)). The brain mask for background field removal was generated by combining a mask from the FMRIB Software Library’s brain extraction tool (FSL BET) ([Smith, 2002](#)) (applied to the last-echo magnitude image) with a mask obtained by thresholding the inverse noise map derived from the non-linear fitting ([Liu et al., 2013](#)) as proposed by [Karsa et al. \(2020\)](#).

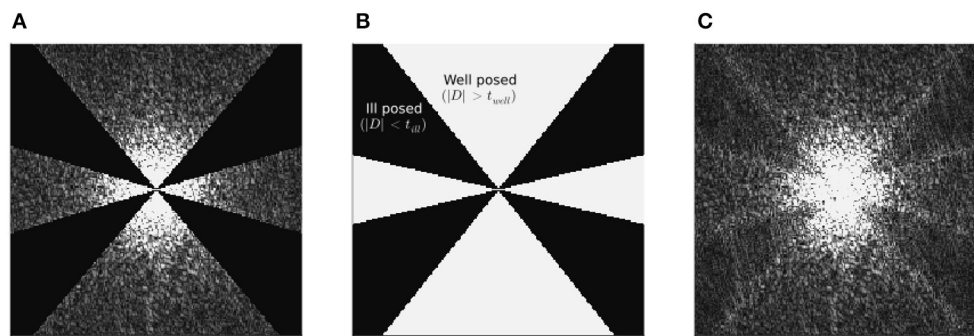


FIGURE 1

Challenge dataset ground truth frequency spectrum (A), together with incomplete spectrum reconstructed k-space (C), using the incomplete spectrum method with the (XSIM-optimal) band limit given in (B). All data are absolute (e.g., $|v|$) and slices are longitudinal (sagittal) in the frequency domain, and with the same grayscale (0...100 [a.u.]). The band limit boundaries, although much less stark than in (A), are still visible in the reconstructed spectrum, which may explain the doubling of streaking artifacts around the calcification in incomplete spectrum QSM reconstructions in Figures 7, 8. The corresponding image space sagittal slice of (C) can be found in Figure 3D.

3.3. Choice of supports

The simulated numerical phantom dataset was used to investigate the effect of the choice of mask S_χ and band-limit S_k on the incomplete spectrum QSM reconstruction.

To illustrate the effect of the band limit on incomplete spectrum reconstruction, in Figure 1 we present a sagittal “slice” in k-space of: the k-space data (v) input into conventional QSM algorithms, the band limit (S_k), and the k-space of the incomplete spectrum QSM reconstruction ($F\chi_{recon}$) corresponding to this band-limit. The reconstructed spectrum shows that the single streak in the input spectrum, which typically results in similar streaks in image space, is essentially split into two streaks at the boundaries of the discarded k-space, after being “filled-in” by the incomplete spectrum approach.

3.3.1. Band-limit

As the purpose here was to choose a frequency domain support to exclude the regions where the QSM inverse problem is ill-posed, the frequency domain was divided into regions where the inverse problem is well-posed and ill-posed following the work of Schweser et al. (2012) and Wu et al. (2012). Fourier space was split into three regions according to the values of the dipole kernel. The well-posed region was defined as the kernel being larger than a threshold t_{well} or $|D| > t_{well}$, and the ill-posed region was defined as $|D|$ smaller than a threshold t_{ill} or $|D| < t_{ill}$, where $t_{ill} \leq t_{well}$. We chose to limit the frequency domain to the well-posed regions, and do not consider a transition region between the thresholds for simplicity, therefore $t_{ill} = t_{well}$. We investigated the relationship between QSM reconstruction quality and frequency domain support (in terms of choice of t_{well}) using the simulated dataset. The image-space support was fixed to the challenge numerical phantom mask described above. The threshold value t_{well} was varied linearly from $\frac{1}{3}$ down to $\frac{1}{1000}$ in 100 steps. Note that we chose $\frac{1}{3}$ as the maximum threshold for the dipole kernel D because, although the absolute value of D has a maximum of $\frac{2}{3}$, using this as a maximum threshold

value would result in a mask of all zeros which would exclude all the data from the inverse problem.

3.3.2. Mask

As previously mentioned, for this incomplete spectrum approach to work, we require both an image space support (or mask) as well as a frequency domain support (or band-limit). As an image space support S_χ , it is straightforward to use the mask that is conventionally used for background field removal in QSM (Schweser et al., 2017). In the case of brain imaging, which is a typical application of QSM, a brain mask can be readily calculated by thresholding one of the magnitude images or applying more sophisticated tools such as FSL BET (Smith, 2002) and noise-based thresholding (Karsa et al., 2020).

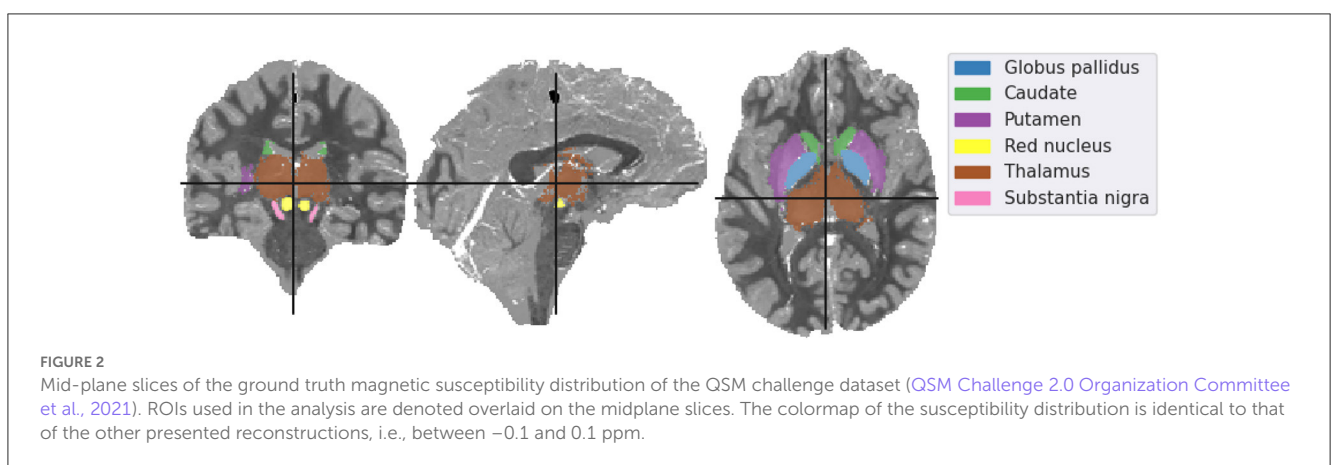
We investigated the effect of dilating and eroding the given binary mask by a few voxels to test the sensitivity of the incomplete spectrum QSM reconstruction to the mask S_χ . In the numerical phantom simulation, we have perfect knowledge of the tissue boundaries and the support of our image-space susceptibility distribution. However, in real life the edges of this mask may not be perfectly determined. Therefore, using the numerical phantom, we explored both erosion as well as dilation of this support. The erosion and dilation were performed with a spherical kernel, ranging in diameter from 1 to 8 voxels. This led to an effective change in the support from -8 to $+8$ voxels. In this investigation the “optimal” band-limit as determined for the original brain mask (see below) was used. Note that in all cases, the input local field map (b) was masked using the same mask (S_χ) as used by the incomplete spectrum algorithm otherwise the underlying assumption for this approach (i.e., $S_\chi \chi = \chi$) would be violated, and this mask was also used when computing the error metrics. We did not have to worry about incorporating erroneous information into the reconstruction as the local phase information is available throughout the domain, since there are no background fields in the simulation.

In the above investigations of the choice of supports (S_χ and S_k) with the numerical phantom, we calculated both the susceptibility tuned XSIM metric from Milovic et al. (2019) used in the QSM

TABLE 1 Reconstruction methods that were compared with the incomplete spectrum approach on the *in vivo* dataset and their parameters tuned for optimal PSNR in the numerical phantom.

Method	Abbreviation	Parameters	XSIM	PSNR
Thresholded k-space division	TKD	Threshold = $\frac{2}{3}$	0.88	39.4
Fast nonlinear susceptibility inversion	FANSI	$\lambda_{TV} = 1 \cdot 10^{-4}$, $\lambda_{TV} = 1 \cdot 10^{-5}$	0.92, 0.94	45.8 , 43.7
Nonlinear dipole inversion	NDI	Early stopping	0.90	40.2
Compressed sensing	CS	$\lambda_{\epsilon_1} = 1 \cdot 10^{-5}$, Ψ : Daubechies 2	0.89	40.6
Incomplete spectrum	IS	$t_{well} = 0.25$	0.88	39.9
Regularized IS	IS reg	$t_{well} = 0.25$, $\lambda_{\epsilon_1} = 1 \cdot 10^{-5}$, Ψ : Daubechies 2	0.89	39.7

Note that the regularized incomplete spectrum approach used the same parameters as the compressed sensing (CS) reconstruction. The XSIM and optimal PSNR in the numerical phantom are given for each reconstruction method. The bold values indicate the best performing algorithms for the respective metric.



challenge 2.0 (QSM Challenge 2.0 Organization Committee et al., 2021), as well as the peak signal to noise ratio (PSNR) given by Korhonen and You (2012). The XSIM metric is defined as

$$XSIM(x, y) = \sum_{ROI} \frac{(2\mu_x\mu_y + K_1)(2\sigma_{xy} + K_2)}{(\mu_x^2 + \mu_y^2 + K_1)(\sigma_x^2 + \sigma_y^2 + K_2)}, \quad (14)$$

where μ_i is the window mean, and σ_i is the window variance (and covariance for σ_{ij}). K_2 and K_1 are constants tuned to $K_1 = 0.01, K_2 = 0.001$ for susceptibility maps. To provide greater sensitivity to structural and local variance errors than other global metrics. We used this XSIM metric specifically because it has been shown to be more resistant to “metric hacking”, i.e. tuning hyperparameters to improve performance with respect to a specific image quality metric, as shown in Milovic et al. (2019) and QSM Challenge 2.0 Organization Committee et al. (2021).

3.4. QSM reconstruction comparison

The incomplete spectrum QSM reconstruction was applied *in vivo* with the threshold value optimized on the QSM Challenge dataset. In both datasets the novel incomplete spectrum method (as well as a compressed sensing regularized version of it) were

compared to four different QSM reconstruction methods chosen from different categories of susceptibility calculation algorithms:

- Thresholded k-space division (TKD) (Shmueli et al., 2009), with point spread function correction for susceptibility underestimation as described by Schweser et al. (2013), was selected as a direct method.
- Non-linear total variation regularization (FANSI) (Milovic et al., 2018) and non-linear dipole inversion (NDI) (Polak et al., 2020) were selected as iterative methods with and without explicit regularization, respectively.
- A generic regularized least squares based compressed sensing reconstruction was used (Lustig et al., 2007).

In the numerical phantom the parameters of these reconstruction methods were tuned as follows, and the results can be found in Table 1.

3.4.1. Parameter optimization for QSM reconstructions

For TKD the theoretical optimum threshold of $\frac{2}{3}$ was used. NDI uses automatic stopping, which requires no tuning. The

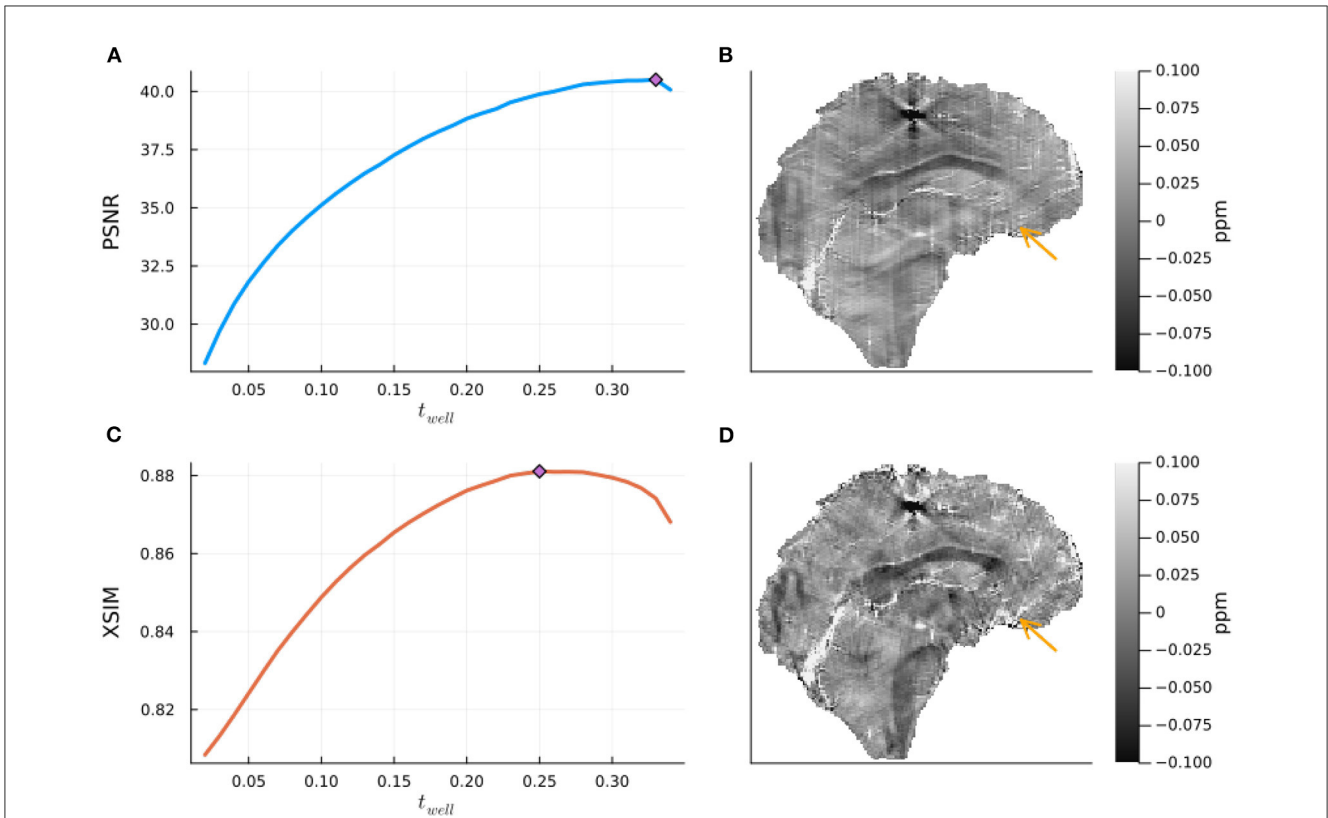


FIGURE 3 The effect of the band-limit S_k on the incomplete spectrum QSM reconstructed in the numerical phantom. On the left are the peak signal to noise Ratio (PSNR) and XSIM metrics for various threshold values t_{well} , computed on the QSM challenge 2.0 dataset 2, with noise level 1 (A, C). On the right are the corresponding optimal reconstructions (with the threshold for optimal PSNR (top) and XSIM (bottom) in a central sagittal slice (B, D). The orange arrow points at a streaking artifact which is successfully suppressed at the higher regularization of the PSNR optimal value.

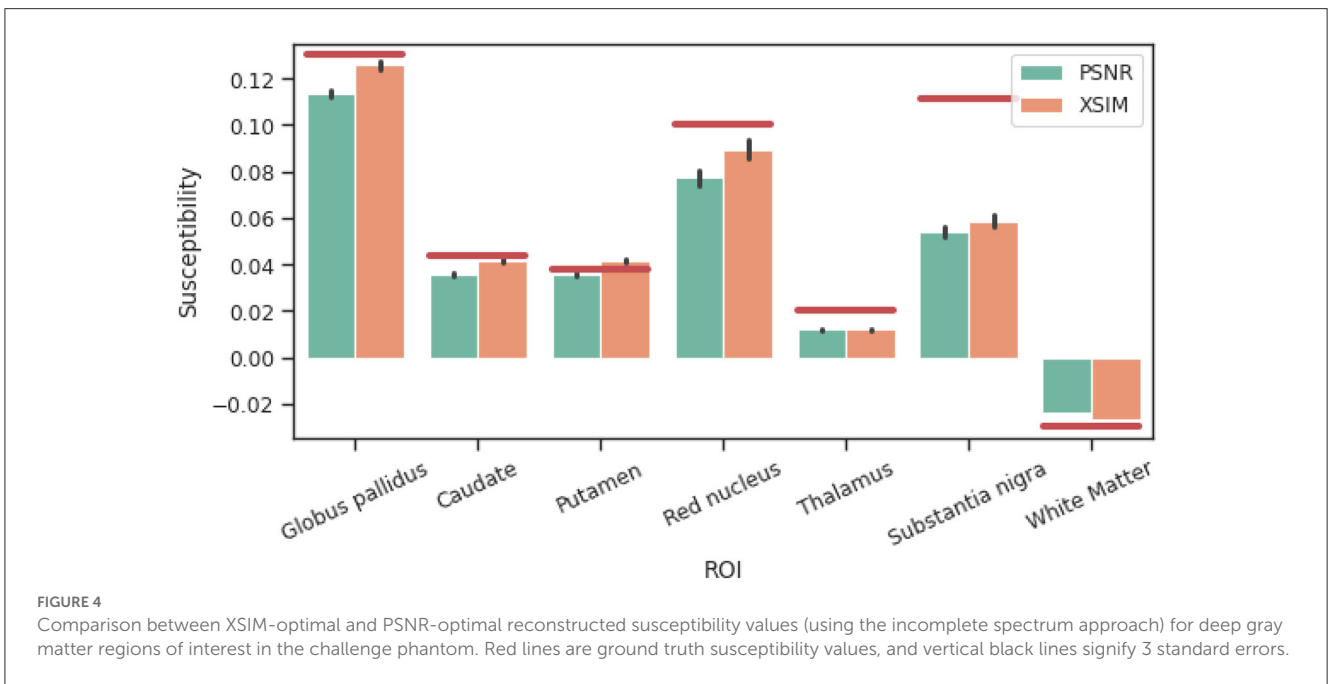


FIGURE 4 Comparison between XSIM-optimal and PSNR-optimal reconstructed susceptibility values (using the incomplete spectrum approach) for deep gray matter regions of interest in the challenge phantom. Red lines are ground truth susceptibility values, and vertical black lines signify 3 standard errors.

compressed sensing and FANSI reconstructions were tuned in the numerical phantom using a parameter sweep to determine the regularization weights for optimal PSNR. For the CS

reconstruction, the same band-limit (S_k) as for the incomplete spectrum approach was used, and only the regularization weight was tuned (using a parameter sweep) for optimal PSNR. This same

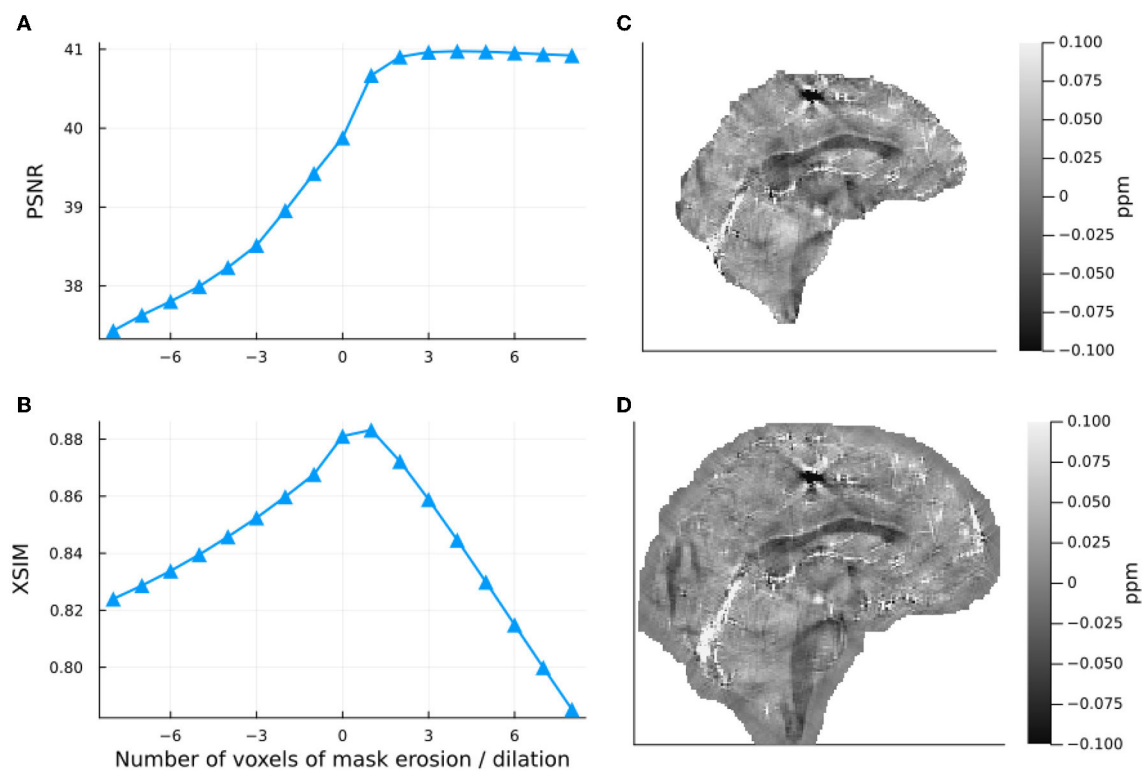


FIGURE 5

Effect of dilation and erosion of the brain mask or image support S_x on the incomplete spectrum QSM reconstructed in the numerical phantom. Input data were masked with the same mask S_x as that used in the reconstruction. On the left-hand side, PSNR (A) and XSIM (B) values are plotted for masks eroded and dilated by different numbers of voxels. The right-hand side shows incomplete spectrum QSM reconstructions with a mask eroded by 5 voxels (C) and a mask dilated by 5 voxels (D).

CS regularization weight was applied to regularize the incomplete spectrum method for ease of comparison.

3.4.2. Region of interest comparison

The mean susceptibility in the globus pallidus, caudate, putamen, red nucleus, thalamus, and substantia nigra were compared across all six different reconstruction methods (i.e. the incomplete spectrum approach, the regularized version, TKD, NDI, nTV and compressed sensing) with the tuned regularization parameters in Table 1. Segmentations of these regions of interest (ROIs) were available for the simulated dataset (see Figure 2), and a segmentation performed using MRI cloud (Miller et al., 2014) was used for each of the volunteer datasets (see Figure 9). ROI mean susceptibility values were compared to the ground truth susceptibility in each ROI and averaged literature values from Bilgic et al. (2012) and Santin et al. (2017) for the numerical phantom and healthy volunteers, respectively.

4. Results

4.1. Choice of supports

The results of the band limit analysis can be found in Figures 3A, C with the sagittal slice of the PSNR-optimal and

XSIM-optimal incomplete spectrum QSM reconstructions shown in Figures 3B, D for comparison. These show the effect on the reconstruction of changing the threshold t_{well} , which changes the size of the well-posed k-space region. The PSNR-optimal reconstruction shows slightly less pronounced streaking artifacts than the XSIM-optimal reconstruction: See for example, the orange arrow in Figures 3B, D. However, the PSNR-optimal reconstruction is smoother and has much lower contrast than the XSIM-optimal reconstruction (Figures 3B, C). This loss in contrast is highlighted when comparing the two reconstructions in the six brain regions of interest, as shown in Figure 4. Based on these results, the XSIM-optimal threshold $t_{\text{well}} = 0.25$ was used for the reconstructions of the *in-vivo* datasets. The results of the space-limit S_x investigation, where the effect of erosion and dilation of the mask are analyzed, are shown in Figure 5.

4.2. Parameter optimization for QSM reconstructions

The PSNR-optimal regularization weight for FANSI was $1 \cdot 10^{-4}$ but this gave over-regularized reconstructions (i.e. smoothed and with loss of contrast) for the *in-vivo* dataset, and was therefore reduced to the XSIM-optimal weight of $1 \cdot 10^{-5}$ which gave acceptable reconstructions with minimal streaking artifacts. Both

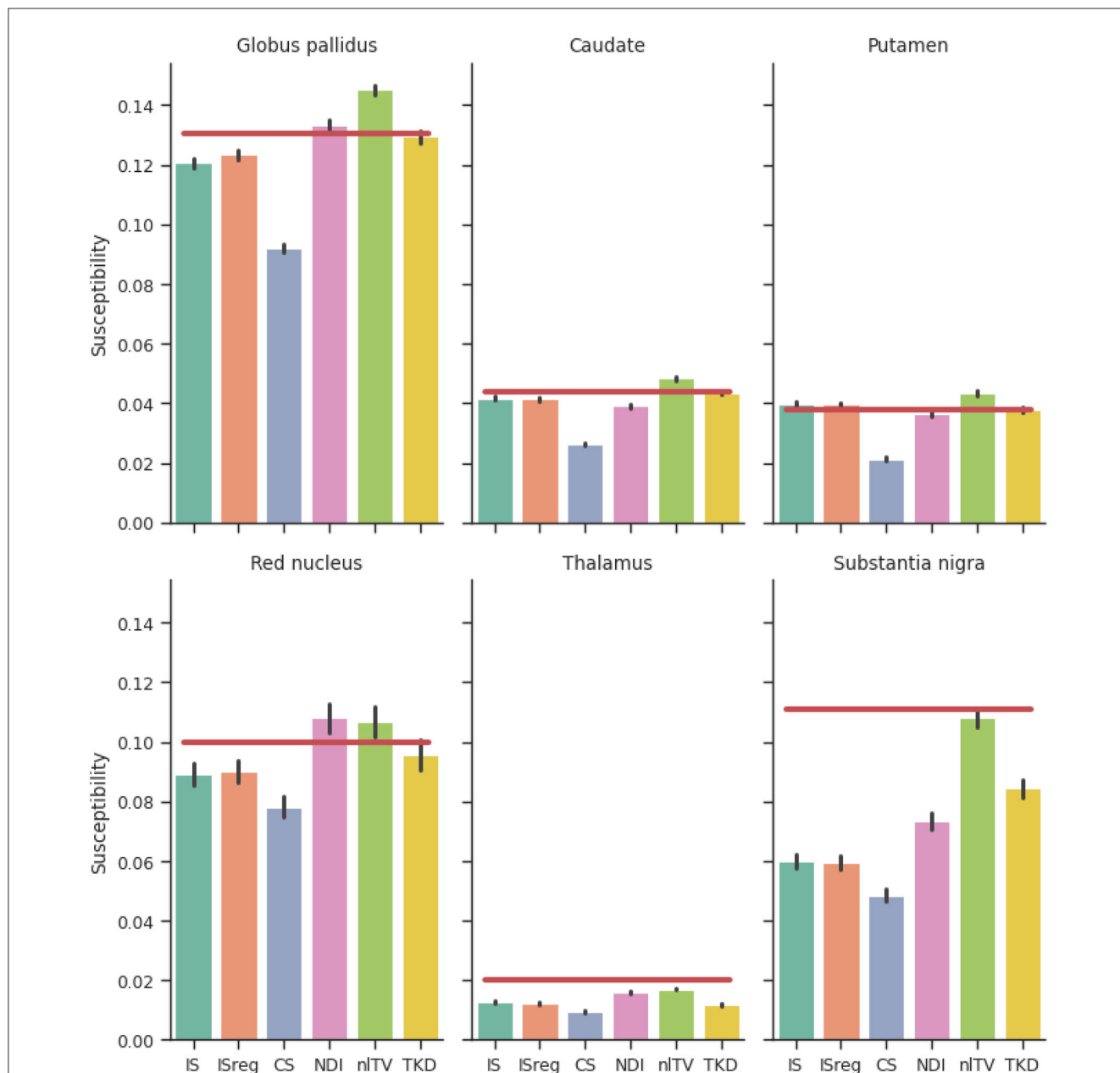


FIGURE 6 Reconstructed susceptibility values of the simulated dataset for deep gray matter regions of interest. Red lines are ground truth susceptibility values, and vertical black lines signify 3 standard errors. IS, Incomplete spectrum ($t_{well} = 0.25$); ISreg, Regularized IS (Same parameters as IS & CS); CS, Compressed sensing (Ψ : Daubechies 2, $\lambda_{\ell_1} = 1 \cdot 10^{-5}$); NDI, Nonlinear Dipole Inversion (w. automatic stopping); FANSI, Fast Nonlinear Susceptibility Inversion ($\lambda_{TV} = 1 \cdot 10^{-5}$); TKD, Thresholded k-space division ($\lambda = 2/3$; w. PSF correction).

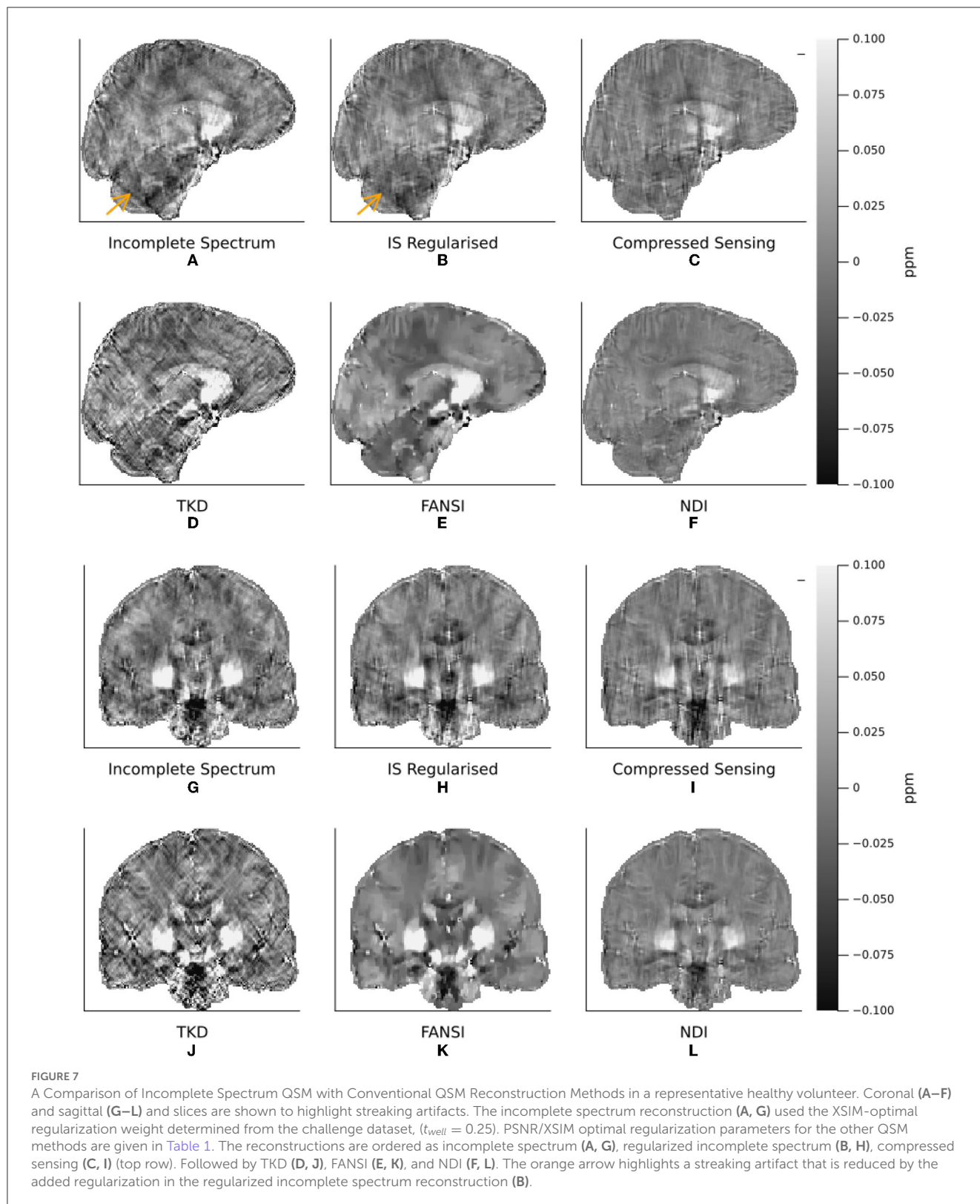
regularization weights are included in Table 1 for reference. The regularization parameters giving optimal PSNR for each method in the numerical phantom are all shown in Table 1. These regularization parameters, tuned in the numerical phantom, were used to reconstruct all the *in-vivo* volunteer data.

4.3. QSM reconstruction comparison

The XSIM and PSNR metrics for all reconstruction methods on the challenge phantom data as well as their parameters can be

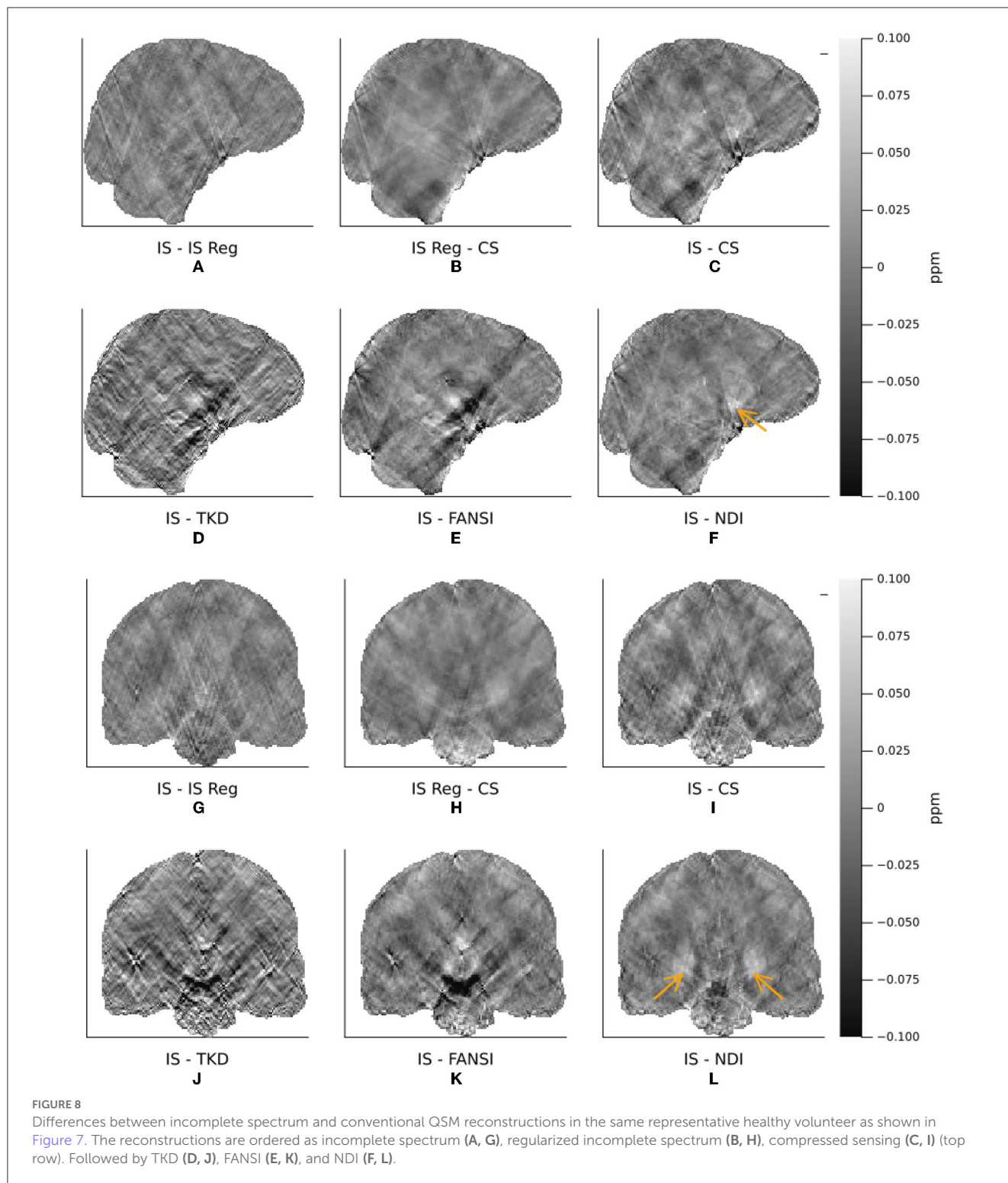
found in Table 1. These metrics show that the incomplete spectrum approach is more accurate, with fewer streaking artifacts than the direct TKD approach. However, the incomplete spectrum approach performs slightly worse than the regularized iterative FANSI and CS methods. The performance of the algorithms are slightly different according to the XSIM and PSNR metrics. Adding regularization to the IS method offers minor improvement to XSIM at the cost of PSNR.

Figure 6 shows a comparison of ROI mean susceptibility values in the simulated phantom for the different QSM reconstruction methods. For reference, ground truth ROI susceptibility values are given by the horizontal red lines.



The XSIM-optimal threshold of $t_{well} = 0.25$ was used in the *in vivo* reconstructions, as it provided higher contrast and less smooth susceptibility maps than the PSNR optimal threshold. All six QSM reconstruction methods are visually compared in Figure 7, where we have displayed sagittal and coronal slices to

emphasize QSM contrast between brain structures typically of interest as well as the level of streaking artifacts. Figure 8 shows difference maps between our proposed incomplete spectrum QSM reconstruction method and the conventional QSM reconstruction methods investigated. The difference maps show that most of the



differences between the conventional QSM reconstructions and the incomplete spectrum reconstruction seem to be residual streaking susceptibility differences and not anatomical artifacts although some deep-brain gray-matter regions appear brighter in the IS QSM, particularly compared with NDI, highlighted by orange arrows in Figures 8F, L.

In Figure 9 the ROI segmentation of a representative healthy volunteer is shown. And Figure 10 shows a comparison of ROI mean susceptibility values, averaged over all five volunteers, for the different QSM reconstruction methods. For reference, literature ROI mean susceptibility values are given by the horizontal red lines.

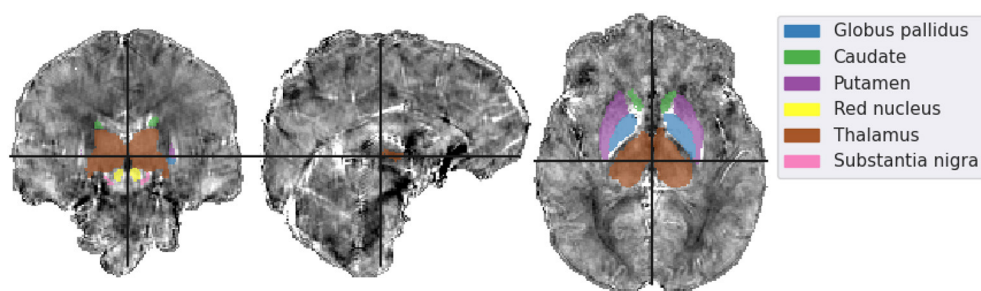


FIGURE 9

Mid-plane slices of the incomplete spectrum reconstruction of the same representative healthy volunteer presented in Figures 7, 8. ROIs segmented using MRI Cloud and used in the analysis are overlaid. The colormap of the susceptibility distribution is identical to that of the other presented reconstructions, i.e., between -0.1 and 0.1 ppm.

5. Discussion and conclusions

Here, we demonstrated a new incomplete spectrum QSM reconstruction approach based on excluding “ill-posed” regions from the frequency domain. Without additional regularization, incomplete spectrum QSM reconstruction showed lower levels of streaking artifacts compared to direct QSM reconstruction and similar accuracy to state-of-the-art QSM reconstruction algorithms.

5.1. Numerical phantom

Investigations in the numerical phantom from the QSM challenge showed that there is a frequency-space band limit S_k that is optimal for this dataset Figure 3, which is relatively robust (a 50% reduction of the threshold resulted in a 7.1 % decrease in the PSNR metric, and decreased the XSIM metric by 2.8%). This XSIM optimal threshold value of $t_{well} = 0.25$ seems high, as it fills in almost two thirds of k-space. The results, however, do not indicate over-regularization (through the loss of anatomical contrast or smoothing), and the incomplete spectrum method provided high-quality reconstructions *in vivo* without requiring additional tuning, further supporting its robustness.

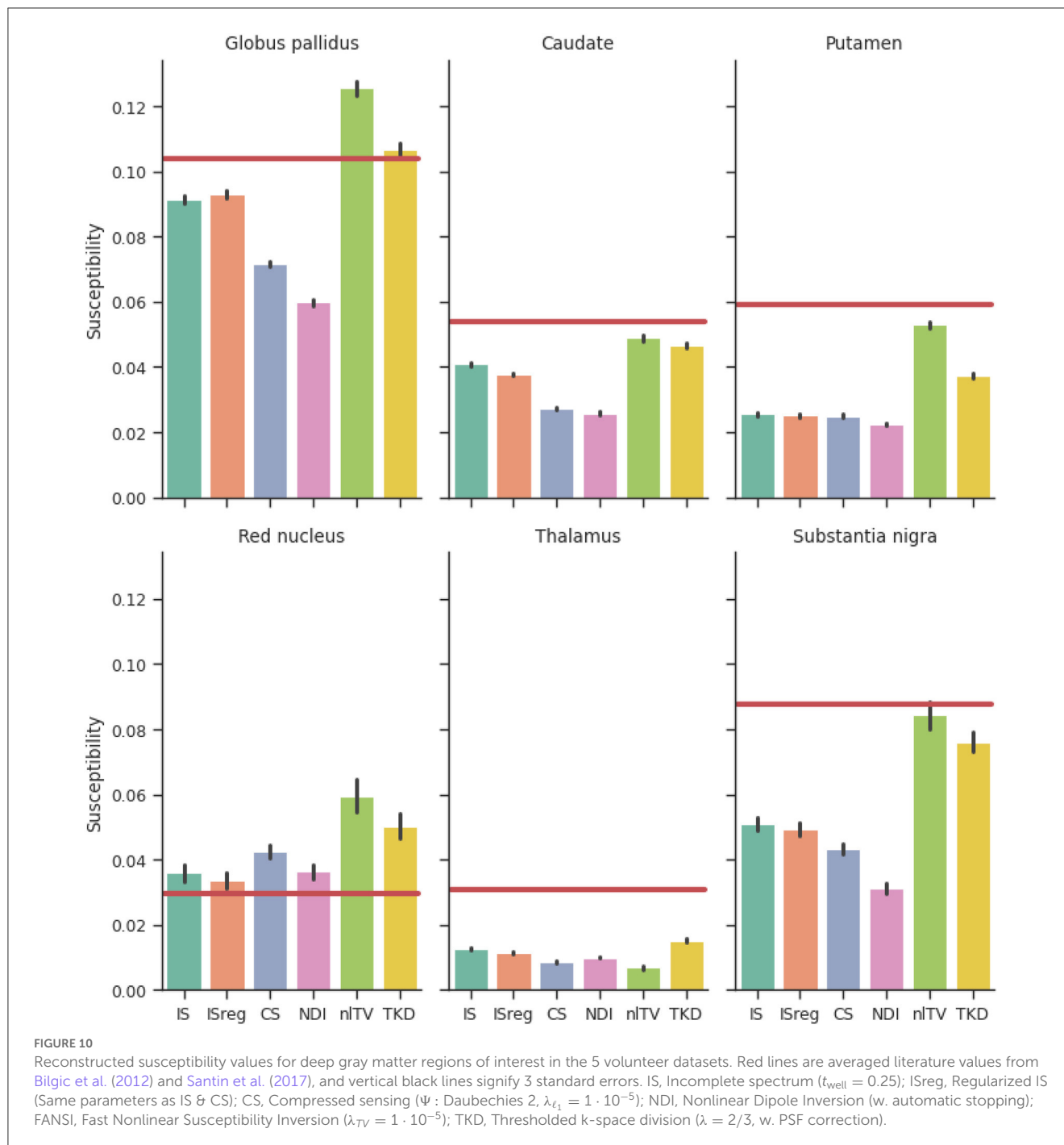
Masking, although non-trivial (Smith, 2002), is already an integral part of most QSM pipelines i.e., for background field removal (Schweser et al., 2017). This means that finding an image support S_x suitable for this incomplete spectrum approach is straightforward. Investigating the effect of eroding and dilating the mask in the numerical phantom showed that using a mask that was slightly larger than the brain region of interest does not negatively affect the QSM reconstruction (actually increasing PSNR in Figure 5). It should be noted, however, that a larger mask slows down the convergence of the method. The reconstruction converged more than twice as fast for 8 voxels of erosion with respect to the original mask: 7.3 seconds compared to 16.2 seconds with no erosion. The decrease in the XSIM metric compared to the PSNR metric as the mask is dilated highlights XSIM's increased sensitivity to local variance error (in this case outside of the original brain mask). Visually, neither the eroded nor the dilated reconstructions feature artifacts related to the choice of mask (see

Figures 5C, D), which demonstrates the IS method to be relatively robust to masking (provided the background field removal was successful for the given mask).

Comparing the reconstructions in the numerical phantom (see Table 1 and Figure 6) we find that the incomplete spectrum performed slightly better than the direct TKD method but worse than the conventional state-of-the-art methods. Since the compressed sensing approach used such a small ℓ_1 penalty term, adding the same regularization term to the incomplete spectrum reconstruction did not improve the metrics, although there is a visual difference between the regularized and unregularized IS reconstructions *in vivo* (see Figures 7A, B, 8). The ROI based analysis (Figure 6) shows a slight underestimation by the incomplete spectrum approach of the mean susceptibility in the globus pallidus (GP), caudate, red nucleus, thalamus and substantia nigra, compared to conventional methods except for the compressed sensing reconstruction which consistently underestimated the mean susceptibility in these ROIs. Overall, NDI performed the best on the challenge phantom as it provides ROI mean susceptibility values closest to the ground truth values except in the substantia nigra (Figure 4). This is not reflected in the XSIM and PSNR metrics (Table 1) nor in the *in-vivo* dataset ROIs (Figure 6), where NDI generally gave the lowest and least accurate reconstructed mean susceptibilities of the algorithms compared.

The “doubling” of the streaking artifact as observed, for example, around the calcification in the top of the brain in the simulated dataset, seems to be a side-effect of the way the incomplete spectrum method reconstructs the missing frequency domain information as illustrated in Figure 1. It is not as apparent *in vivo*, most likely because this dataset has a lower overall SNR. Since this IS method fills in k-space information between cones at two angles centered on the origin it replaces more high frequency than low frequency information, leading to a minor denoising effect (observable as smoothing, specifically when comparing the *in vivo* TKD and incomplete spectrum reconstructions).

Since the incomplete spectrum method presented here does not rescale regions of the frequency domain (like TKD), it does not directly change the point spread function of the operator, and no rescaling of the output susceptibility map should be necessary [as was proposed for TKD by Schweser et al. (2013)]. This is supported by the incomplete spectrum results on the simulated dataset where



no scaling in contrast was observed for higher levels of (intrinsic) regularization (although a slight loss in contrast due to smoothing was observed, as in the comparison between XSIM-optimal and PSNR-optimal reconstructions shown in Figures 3, 4).

5.2. *In vivo* reconstructions

Figure 10 shows that, *in vivo*, the incomplete spectrum approach gave ROI mean susceptibility values similar to those from commonly used, state-of-the-art algorithms i.e., NDI and

nITV. This suggests that the incomplete spectrum method did not systematically overestimate or underestimate the susceptibilities in these ROIs. In most of the ROIs, the incomplete spectrum approach gave susceptibility values between those from nITV and TKD. The compressed sensing reconstruction gave the lowest susceptibility values in all ROIs. The literature values were larger than the values reconstructed by all algorithms in the caudate, putamen, substantia nigra (and globus pallidus) perhaps because the healthy volunteers were relatively young compared to the subjects included in the studies cited here and may, therefore, have had a lower iron content and a lower susceptibility in these deep-brain gray matter ROIs

than the subjects in the cited studies (Li et al., 2014, 2023; Zhang et al., 2018).

With additional ℓ_1 wavelet regularization, the incomplete spectrum QSM reconstruction more closely resembles the compressed sensing QSM (Wu et al., 2012) (Figures 7A–C, G–I, 8B, C, H, I). At high levels of regularization the regularized incomplete spectrum and compressed sensing reconstructions become identical, as expected from their similar cost functions (see Equations 12, 13), and illustrated in Supplementary Figure S1. Adding the regularization to the incomplete spectrum approach leads to less pronounced streaking (as illustrated by the orange arrow, Figures 7A, B). However, regularization adds another parameter to the method which then requires tuning, as opposed to the original implementation which is less sensitive to t_{well} initially tuned on the numerical phantom. Further, it has been shown that band-limiting based on thresholding the dipole kernel as performed in this incomplete spectrum approach leads to correlated artifacts (Wu et al., 2012) thereby violating the assumptions of compressed sensing (i.e. uncorrelated artifacts). Therefore, additional regularization using this compressed sensing term is disadvantageous compared to the original unregularized incomplete spectrum approach.

The biggest limitation of the incomplete spectrum QSM reconstruction approach lies in the input data $v = D^{-1}Fb$, which is the directly deconvolved phase information. Streaking artifacts are introduced by multiplication with the inverse dipole kernel D^{-1} and the incomplete spectrum method then “corrects” for these. Future work will involve applying the incomplete spectrum method to reconstructed susceptibility maps, to provide additional “correction” of the spectrum where applicable. This could lead to frequency domain correction schemes that would work in tandem with conventional iterative methods to improve the robustness to noise, or artifacts that can be identified in specific regions of frequency domain (such as streaking). This technique provides a new tool for filling in missing regions of frequency space, or correcting “ill-posed” or noisy frequency-space regions with a suitable band-limit in QSM maps by using an image space mask.

Data availability statement

The data analyzed in this study is subject to the following licenses/restrictions: the anonymized *in-vivo* dataset and analysis will be provided by the authors upon reasonable request. Requests to access these datasets should be directed to KS, k.shmueli@ucl.ac.uk.

Ethics statement

Ethical review and approval was not required for the study on human participants in accordance with the local legislation

and institutional requirements. Written informed consent for participation was not required for this study in accordance with the national legislation and the institutional requirements.

Author contributions

PF contributed to the conception and design of the study and performed the numerical analysis. KS was responsible for funding the research and gave feedback on the analysis. All authors contributed to manuscript writing and editing, as well as reading and approving the submitted version.

Funding

The authors are funded by ERC Consolidator Grant DiSCo MRI SFN 770939.

Acknowledgments

The authors would like to thank Dr. Anita Karsa for acquiring the *in vivo* data used in this study.

Conflict of interest

The authors declare that the research was conducted in the absence of any commercial or financial relationships that could be construed as a potential conflict of interest.

Publisher's note

All claims expressed in this article are solely those of the authors and do not necessarily represent those of their affiliated organizations, or those of the publisher, the editors and the reviewers. Any product that may be evaluated in this article, or claim that may be made by its manufacturer, is not guaranteed or endorsed by the publisher.

Supplementary material

The Supplementary Material for this article can be found online at: <https://www.frontiersin.org/articles/10.3389/fnins.2023.1130524/full#supplementary-material>

References

- Bilgic, B., Pfefferbaum, A., Rohlfing, T., Sullivan, E. V., and Adalsteinsson, E. (2012). Mri estimates of brain iron concentration in normal aging using quantitative susceptibility mapping. *NeuroImage* 59, 2625–2635. doi: 10.1016/j.neuroimage.2011.08.077
- Bollmann, S., Rasmussen, K. G. B., Kristensen, M., Blendal, R. G., Østergaard, L. R., Plocharski, M., et al. (2019). DeepQSM-using deep learning to solve the dipole inversion for quantitative susceptibility mapping. *Neuroimage* 195, 373–383. doi: 10.1016/j.neuroimage.2019.03.060
- Deistung, A., Schweser, F., and Reichenbach, J. R. (2017). Overview of quantitative susceptibility mapping. *NMR in Biomed.* 30, e3569. doi: 10.1002/nbm.3569
- den Bouter, M. L., van den Berg, P. M., and Remis, R. F. (2021). Inversion of incomplete spectral data using support information with an application to magnetic resonance imaging. *J. Phys. Commun.* 5, 055006. doi: 10.1088/2399-6528/abfd45
- Fuks, B. A. (1963). *Theory of Analytic Functions of Several Complex Variables*. Rhode Island: American Mathematical Soc. doi: 10.1090/mmono/008
- Jung, W., Bollmann, S., and Lee, J. (2022). Overview of quantitative susceptibility mapping using deep learning: Current status, challenges and opportunities. *NMR in Biomed.* 35, e4292. doi: 10.1002/nbm.4292
- Jung, W., Yoon, J., Ji, S., Choi, J. Y., Kim, J. M., Nam, Y., et al. (2020). Exploring linearity of deep neural network trained QSM: QSMnet+. *Neuroimage* 211, 116619. doi: 10.1016/j.neuroimage.2020.116619
- Karsa, A., Punwani, S., and Shmueli, K. (2019). The effect of low resolution and coverage on the accuracy of susceptibility mapping. *Magn. Reson. Med.* 81, 1833–1848. doi: 10.1002/mrm.27542
- Karsa, A., Punwani, S., and Shmueli, K. (2020). An optimized and highly repeatable mri acquisition and processing pipeline for quantitative susceptibility mapping in the head-and-neck region. *Magn. Reson. Med.* 84, 3206–3222. doi: 10.1002/mrm.28377
- Kee, Y., Liu, Z., Zhou, L., Dimov, A., Cho, J., de Rochefort, L., et al. (2017). Quantitative susceptibility mapping (qsm) algorithms: Mathematical rationale and computational implementations. *IEEE Trans. Biomed. Eng.* 64, 2531–2545. doi: 10.1109/TBME.2017.2749298
- Kiernowski, O. C., Karsa, A., Wastling, S. J., Thornton, J. S., and Shmueli, K. (2022). Investigating the effect of oblique image acquisition on the accuracy of qsm and a robust tilt correction method. *Magn. Reson. Med.* 89, 1791–1808. doi: 10.1002/mrm.29550
- Knopp, T., and Grosser, M. (2021). Mrircore.jl: An mri reconstruction framework written in julia. *Magn. Reson. Med.* 86, 1633–1646. doi: 10.1002/mrm.28792
- Korhonen, J., and You, J. (2012). “Peak signal-to-noise ratio revisited: Is simple beautiful?” in *2012 Fourth International Workshop on Quality of Multimedia Experience (IQQE)* (IEEE) 37–38. doi: 10.1109/QoMEX.2012.6263880
- Li, G., Tong, R., Zhang, M., Gillen, K. M., Jiang, W., Du, Y., et al. (2023). Age-dependent changes in brain iron deposition and volume in deep gray matter nuclei using quantitative susceptibility mapping. *NeuroImage* 269, 119923. doi: 10.1016/j.neuroimage.2023.119923
- Li, W., Wu, B., Batrachenko, A., Bancroft-Wu, V., Morey, R. A., Shashi, V., et al. (2014). Differential developmental trajectories of magnetic susceptibility in human brain gray and white matter over the lifespan. *Human Brain Mapp.* 35, 2698–2713. doi: 10.1002/hbm.22360
- Liu, T., Khalidov, I., de Rochefort, L., Spincemaille, P., Liu, J., Tsiouris, A. J., et al. (2011). A novel background field removal method for mri using projection onto dipole fields (pdf). *NMR Biomed.* 24, 1129–1136. doi: 10.1002/nbm.1670
- Liu, T., Wisnieff, C., Lou, M., Chen, W., Spincemaille, P., and Wang, Y. (2013). Nonlinear formulation of the magnetic field to source relationship for robust quantitative susceptibility mapping. *Magn. Reson. Med.* 69, 467–476. doi: 10.1002/mrm.24272
- Lustig, M., Donoho, D., and Pauly, J. M. (2007). Sparse mri: The application of compressed sensing for rapid mr imaging. *Magn. Reson. Med.* 58, 1182–1195. doi: 10.1002/mrm.21391
- Majumdar, A., and Ward, R. K. (2012). On the choice of compressed sensing priors and sparsifying transforms for mr image reconstruction: an experimental study. *Signal Proces.* 27, 1035–1048. doi: 10.1016/j.ijimage.2012.08.002
- Marques, J., and Bowtell, R. (2005). Application of a fourier-based method for rapid calculation of field inhomogeneity due to spatial variation of magnetic susceptibility. *Concepts Magn. Reson. Part B* 25B, 65–78. doi: 10.1002/cmr.b.20034
- Marques, J. P., Meineke, J., Milovic, C., Bilgic, B., Chan, K.-S., Hedouin, R., et al. (2021). Qsm reconstruction challenge 2.0: A realistic in silico head phantom for mri data simulation and evaluation of susceptibility mapping procedures. *Magn. Reson. Med.* 86, 526–542. doi: 10.1002/mrm.28716
- Miller, M. I., Younes, L., and Trounev, A. (2014). Diffeomorphometry and geodesic positioning systems for human anatomy. *Technology* 2, 36–43. doi: 10.1142/S2339547814500010
- Milovic, C., Bilgic, B., Zhao, B., Acosta-Cabronero, J., and Tejos, C. (2018). Fast nonlinear susceptibility inversion with variational regularization. *Magn. Reson. Med.* 80, 814–821. doi: 10.1002/mrm.27073
- Milovic, C., Tejos, C., and Irarrazaval, P. (2019). “Structural similarity index metric setup for qsm applications (xsim),” in *5th International Workshop on MRI Phase Contrast Quantitative Susceptibility Mapping* (Seoul, Korea).
- Papoulis, A. (1975). A new algorithm in spectral analysis and band-limited extrapolation. *IEEE Trans. Circ. Syst.* 22, 735–742. doi: 10.1109/TCS.1975.1084118
- Polak, D., Chatnuntawech, I., Yoon, J., Iyer, S. S., Milovic, C., Lee, J., et al. (2020). Nonlinear dipole inversion (ndi) enables robust quantitative susceptibility mapping (qsm). *NMR Biomed.* 33, e4271. doi: 10.1002/nbm.4271
- QSM Challenge 2.0 Organization Committee, Bilgic, B., Langkammer, C., Marques, J. P., Meineke, J., Milovic, C., et al. (2021). Qsm reconstruction challenge 2.0: Design and report of results. *Magn. Reson. Med.* 86, 1241–1255. doi: 10.1002/mrm.28754
- Rhebergen, J. B., van den Berg, P. M., and Habashy, T. M. (1997). Iterative reconstruction of images from incomplete spectral data. *Inverse Problems* 13, 829. doi: 10.1088/0266-5611/13/3/017
- Salomir, R., de Senneville, B. D., and Moonen, C. T. (2003). A fast calculation method for magnetic field inhomogeneity due to an arbitrary distribution of bulk susceptibility. *Concepts Magn. Reson. B* 19, 26–34. doi: 10.1002/cmr.b.10083
- Santin, M. D., Didier, M., Valabrègue, R., Yahia Cherif, L., García-Lorenzo, D., Loureiro de Sousa, P., et al. (2017). Reproducibility of r2* and quantitative susceptibility mapping (qsm) reconstruction methods in the basal ganglia of healthy subjects. *NMR Biomed.* 30, e3491. doi: 10.1002/nbm.3491
- Schweser, F., Sommer, K., Deistung, A., and Reichenbach, J. R. (2012). Quantitative susceptibility mapping for investigating subtle susceptibility variations in the human brain. *Neuroimage* 62, 2083–2100. doi: 10.1016/j.neuroimage.2012.05.067
- Schweser, F., Deistung, A., Sommer, K., and Reichenbach, J. R. (2013). Toward online reconstruction of quantitative susceptibility maps: superfast dipole inversion. *Magn. Reson. Med.* 69, 1581–1593. doi: 10.1002/mrm.24405
- Schweser, F., Robinson, S. D., de Rochefort, L., Li, W., and Bredies, K. (2017). An illustrated comparison of preprocessing methods for phase mri and qsm: removal of background field contributions from sources outside the region of interest. *NMR Biomed.* 30, e3604. doi: 10.1002/nbm.3604
- Shmueli, K. (2020). “Chapter 31 - quantitative susceptibility mapping,” in *Quantitative Magnetic Resonance Imaging, volume 1 of Advances in Magnetic Resonance Technology and Applications*, eds. N., Seiberlich, V., Gulani, F., Calamante, A., Campbell-Washburn, M., Doneva, H. H., Hu, et al. (New York: Academic Press) 819–838. doi: 10.1016/B978-0-12-817057-1.00033-0
- Shmueli, K., de Zwart, J. A., van Gelderen, P., Li, T.-Q., Dodd, S. J., and Duyn, J. H. (2009). Magnetic susceptibility mapping of brain tissue in vivo using mri phase data. *Magn. Reson. Med.* 62, 1510–1522. doi: 10.1002/mrm.22135
- Smith, S. M. (2002). Fast robust automated brain extraction. *Human Brain Mapping* 17, 143–155. doi: 10.1002/hbm.10062
- Strang, G. (2019). *Linear Algebra and Learning From Data, volume 4*. Cambridge: Wellesley-Cambridge Press.
- Vonesch, C., Blu, T., and Unser, M. (2007). Generalized daubechies wavelet families. *IEEE Trans. Signal Proc.* 55, 4415–4429. doi: 10.1109/TSP.2007.896255
- Wang, Y., and Liu, T. (2015). Quantitative susceptibility mapping (qsm): Decoding mri data for a tissue magnetic biomarker. *Magn. Reson. Med.* 73, 82–101. doi: 10.1002/mrm.25358
- Wu, B., Li, W., Guidon, A., and Liu, C. (2012). Whole brain susceptibility mapping using compressed sensing. *Magn. Reson. Med.* 67, 137–147. doi: 10.1002/mrm.23000
- Zhang, Y., Wei, H., Cronin, M. J., He, N., Yan, F., and Liu, C. (2018). Longitudinal atlas for normative human brain development and aging over the lifespan using quantitative susceptibility mapping. *NeuroImage* 171, 176–189. doi: 10.1016/j.neuroimage.2018.01.008